

Effect of accelerating voltages on indexing of SEM-EBSD via pattern matching

Tomotaka Hatakeyama^{*}, Kota Sawada

Research Center for Structural Materials, National Institute for Materials Science, Japan

ARTICLE INFO

Keywords:

Electron backscattered diffraction
Pattern matching
Spherical indexing
Accelerating voltage
Special resolution

ABSTRACT

The influence of the accelerating voltage on the spatial resolution and phase indexing accuracy of electron backscattered diffraction (SEM-EBSD) was systematically investigated using austenitic heat-resistant steel. Both traditional Hough transformation and novel Spherical Indexing methods were employed to analyze the kernel average misorientation (KAM) and indexing of fine $M_{23}C_6$ precipitates. It was confirmed that lower accelerating voltages reduce the interaction volume, thereby improving the spatial resolution. Spherical Indexing provided enhanced accuracy in detecting local misorientations, especially in the creep-ruptured material. While the effect of the accelerating voltage on KAM was minimal, it became significant when indexing fine precipitates. At 10 kV, precipitates as small as 50 nm on the $\Sigma 3$ boundaries could be indexed, whereas precipitates of 200 nm at 15 kV and 300 nm at 25 kV were required for reliable identification. These results demonstrate the critical role of measurement conditions in advanced EBSD microstructural characterization and suggest the effectiveness of Spherical Indexing for high-resolution evaluation of creep damage and phase separation of nanoscale features.

1. Introduction

Electron backscattered diffraction (EBSD), combined with scanning electron microscopy (SEM) is widely used for microstructural analysis of metallic materials [1]. In EBSD, patterns generated by the diffraction of incident electrons at the crystal planes near the specimen surface are acquired, and the crystal orientation at each measurement point is determined by indexing. By scanning the electron beam in a grid at an arbitrary step size and analyzing the resulting map of the crystal orientations, various microstructural factors can be quantitatively evaluated. For example, the average misorientation between a measurement point and its adjacent points is defined as the kernel average misorientation (KAM). Since dislocation introduction causes crystal rotation, there is a correlation between the creep strain and the average value of KAM. Based on this relationship, creep damage evaluation methods of austenitic heat-resistant steels used for power plant components have been investigated [2–7].

For indexing the EBSD patterns, lines (bands: corresponding to crystallographic planes) in the pattern image are detected using the Hough transformation, which converts them into points in the Hough space [8]. However, since the Hough-transformed “points” have size, traditional indexing results are affected by unavoidable errors of

approximately one degree [9]. While this error does not pose issues for grain boundary detection or texture evaluation via EBSD, it becomes significant when analyzing KAM values of less than one degree for creep damage evaluation. Although several algorithms have been developed to improve angular resolution (e.g., high-resolution (HR)-EBSD [10] and *PyEBSDIndex* [11]), they still have some limitations.

Recently, Spherical Indexing has been developed, which indexes EBSD patterns by pattern matching between simulated and experimental EBSD patterns [12,13]. One feature of this method is that KAM values with extremely small measurement errors can be obtained [14]. Hatakeyama et al. reported that KAM obtained by Spherical Indexing enabled high-precision creep damage evaluation, especially in low-strain regions where conventional Hough transformation methods were adversely affected by error [15]. Thus, with the advent of Spherical Indexing, microstructural analysis using EBSD is expected to advance further.

The orientation indicated by the EBSD pattern represents the average value over the region where the pattern is generated by electron diffraction. In SEM-EBSD, the detected EBSD pattern is considered to originate from a region approximately 40–70 nm beneath the surface. Although the spatial resolution of SEM-EBSD depends on measurement conditions, it is reported that the resolution is tens of nm laterally [16]. At a specimen tilt angle of 70°, the vertical spatial resolution is

^{*} Corresponding author.

E-mail address: hatakeyama.tomotaka@nims.go.jp (T. Hatakeyama).

<https://doi.org/10.1016/j.ultramic.2026.114387>

Received 25 November 2025; Received in revised form 15 April 2026; Accepted 15 May 2026

Available online 16 May 2026

0304-3991/© 2026 The Authors. Published by Elsevier B.V. This is an open access article under the CC BY license (<http://creativecommons.org/licenses/by/4.0/>).

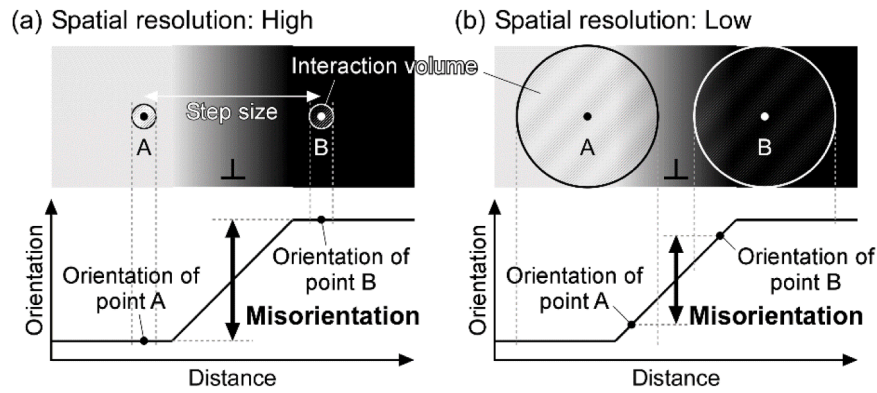


Fig. 1. Schematic illustration of the effect of interaction volume on the misorientation measurement of the neighboring pixels when interaction volume is (a) small and (b) large.

(a) Spatial resolution: High (b) Spatial resolution: Low

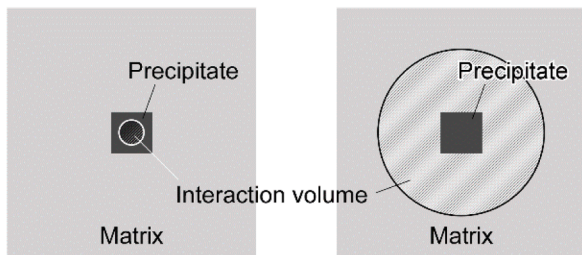


Fig. 2. Schematic illustration of the relationship between interaction volume and precipitate size when interaction volume is (a) small and (b) large.

geometrically approximately three times greater than the lateral resolution [16]. When considering crystal rotation caused by dislocations, if the interaction volume is sufficiently small compared to the orientation change in the specimen, accurate misorientation evaluation is possible, as shown in Fig. 1(a). However, if the interaction volume is large, as in Fig. 1(b), the misorientation may be underestimated owing to the averaging of orientation changes. While conventional Hough transformation indexing does not have sufficient sensitivity to detect this difference, Spherical Indexing may be capable of detecting such minute local misorientations.

Since diffraction planes change based on the crystal structure, phase separation can also be achieved from EBSD patterns [17–19]. If precipitates can be indexed, their deformation and fracture behavior can be discussed in relation to their orientation relationship with the matrix [17]. Regarding phase separation, Spherical Indexing, which utilizes matching of the entire pattern, may be superior to the Hough transformation, which relies only on the angular relationships of the detected bands. When indexing fine precipitates, analysis is possible if the precipitate is larger than the interaction volume (Fig. 2(a)). However, indexing of fine precipitates becomes difficult [20] if the interaction volume is larger than that of the precipitate, because the matrix pattern prevails (Fig. 2(b)).

To fully utilize the newly developed Spherical Indexing technique, it is necessary to accumulate fundamental knowledge regarding measurement conditions. From the perspectives of local misorientation evaluation and phase separation, insights into the influence of SEM-EBSD spatial resolution on indexing results are required. The spatial resolution of SEM-EBSD has been reported to vary with accelerating voltage [16]. Although the probe current also affects spatial resolution, the impact of the accelerating voltage is more pronounced [16]. Therefore, in this study, we investigated how spatial resolution changes with accelerating voltage and examined its influence on KAM obtained using Spherical Indexing as well as on phase separation of fine

Table 1

SEM-EBSD measurement conditions for each accelerating voltage.

Accelerating voltage [kV]	10	15	20	25
Working distance [mm]	20	20	20	20
Aperture [μm]	120	120	120	120
Exposure time [ms]	4	2	2	2
Scan speed [fps]	250	500	500	500

precipitates.

2. Experimental procedures

The sample used in this study was 25Cr-20Ni-Nb-N steel (KA-SUS310J1TB) solution treated at 1503 K (virgin sample) [21]. This steel is an austenitic heat-resistant steel used for thermal power plants. The virgin sample was aged at 923 K for 500 h in air, followed by creep testing at 873 K and 280 MPa in air. The rupture time was 2812.9 h (creep-ruptured sample) [17]. The virgin sample and gauge portion of creep-ruptured sample were sectioned, polished using abrasive paper, diamond paste, and colloidal silica, and subsequently subjected to SEM and SEM-EBSD observations.

For SEM observation, an Auriga Laser (ZEISS) was utilized. Inlens secondary electron (SE) images were acquired at an accelerating voltage of 2 kV and working distance (WD) of 5 mm. EBSD patterns were obtained on a hexagonal grid using an Orion detector (EDAX) attached to the same SEM. The accelerating voltage for EBSD analysis varied as 10, 15, 20, and 25 kV. In all measurements, the WD, aperture, and binning were fixed at 20 mm, 120 μm , and 4×4 (image size: 160×120), respectively. The EBSD measurement conditions for each accelerating voltage are summarized in Table 1. At 10 kV, the exposure time was doubled to ensure sufficient brightness of the EBSD patterns for indexing. All acquired EBSD patterns were saved as 8-bit images for subsequent analysis.

Master patterns were generated for each accelerating voltage using OIM Analysis 9 and OIM Matrix (EDAX). The master pattern of the austenite matrix was simulated using dynamical diffraction theory [22, 23], assuming a face-centered cubic (fcc, space group: Fm-3m) structure with a lattice constant of 0.3599 nm [14]. Dynamical theory was selected for the austenite matrix to perform a precise misorientation analysis, as it reproduces an accurate master pattern close to the experimental pattern. In contrast, the master pattern of the M_{23}C_6 precipitate was simulated using kinematical diffraction theory to reduce computational cost, assuming a face-centered cubic (fcc, space group: Fm-3m) structure with a lattice constant of 1.077 nm. These master patterns were used for re-indexing the EBSD patterns via Spherical Indexing.

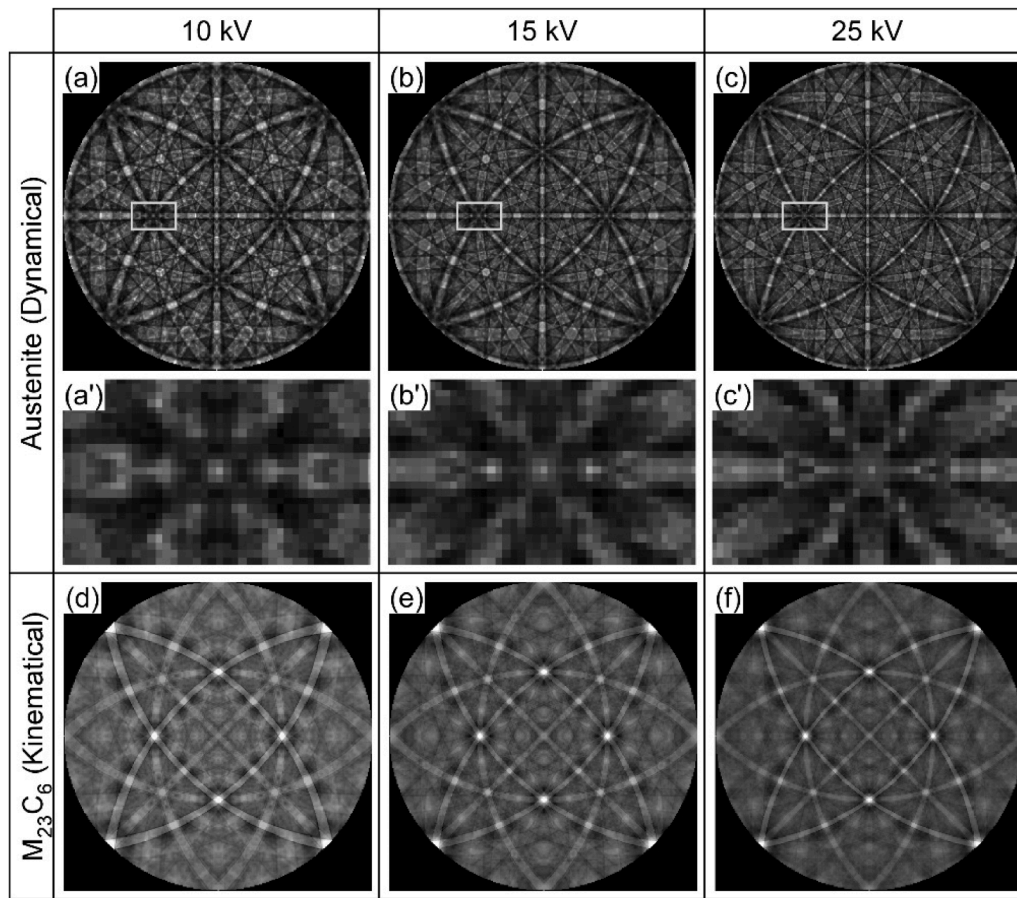


Fig. 3. Spherical master patterns of (a)–(c) austenite and (d)–(f) $M_{23}C_6$ generated by dynamical and kinematical simulations, respectively, with accelerating voltages of (a)(d) 10, (b)(e) 15, and (c)(f) 25 kV. (a')–(c') are the enlarged view of rectangles in (a)–(c).

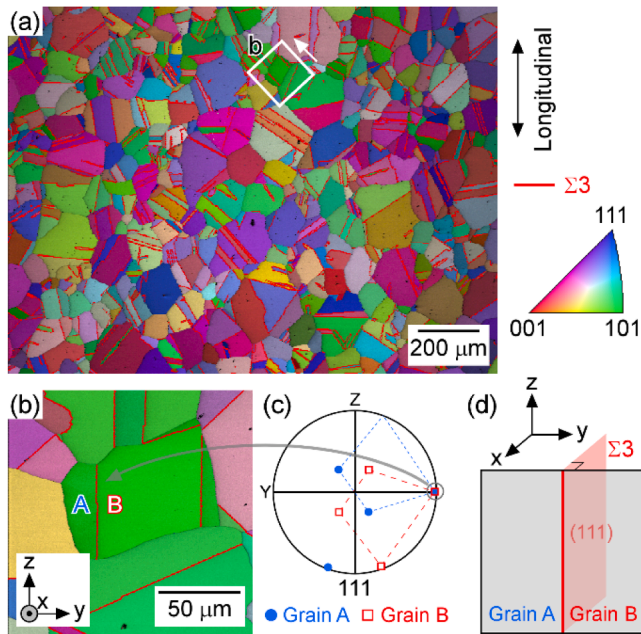


Fig. 4. (a)(b) IPF map of virgin sample, (c) pole figure for 111, and (d) schematic illustration of the grain boundary geometry between grain A and grain B in (b).

3. Results and discussion

3.1. Effect of accelerating voltage on EBSD pattern formation

In 25Cr-20Ni-Nb-N steel, $M_{23}C_6$ precipitates during aging and creep [24,25]. To conduct phase separation between the austenite matrix and $M_{23}C_6$ using Spherical Indexing, master patterns were generated at various accelerating voltages, as shown in Fig. 3. As is evident from the enlarged master patterns in Fig. 3(a')–(c'), higher accelerating voltages result in narrower width of bands. The bands in the EBSD patterns were formed by diffraction from the crystal planes near the specimen surface. The width of the bands is determined by the geometric relationship between the diffraction angle θ given by Bragg's law ($2d\sin\theta = \lambda$) and the distance from the measurement point to the phosphor screen [14]. As the accelerating voltage increased, the wavelength λ of the electron beam decreased. Since the interplanar spacing d remains constant, the diffraction angle θ becomes smaller, resulting in a narrower width of bands.

3.2. Effect of accelerating voltage on spatial resolution

It is known that the spatial resolution of EBSD changes with the accelerating voltage of the SEM [16]. However, it is difficult to directly measure the spatial resolution of EBSD. In this study, the $\Sigma 3$ coherent twin boundary in austenitic steel, where the boundary plane is (111), was utilized. Fig. 4(a) shows an inverse pole figure (IPF) map of the virgin sample acquired at an accelerating voltage of 15 kV. The red lines in the figure represent the $\Sigma 3$ boundaries. From the state in which Fig. 4(a) was measured, an IPF map of the region within the white box was acquired by rotating the sample stage such that the arrow moved

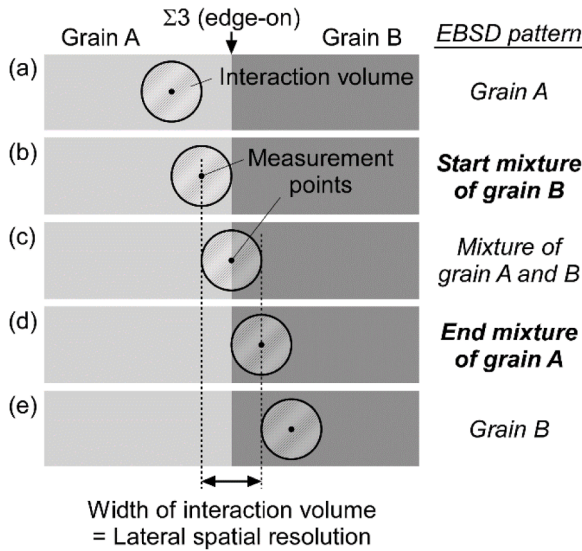


Fig. 5. Schematic illustration of the relationship between interaction volume and distance from the grain boundary.

upward, as shown in Fig. 4(b). The $\Sigma 3$ boundary can be observed along the vertical direction in the figure. Fig. 4(c) shows the $\{111\}$ pole figure for grains A and B from Fig. 4(b). Because $\{111\}$ of both grains A and B overlapped in the vicinity of the great circle (approximately 89° from the sample normal), it was suggested that both grains shared the $\{111\}$ at their interface. In other words, the $\Sigma 3$ boundary was oriented edge-on [26] (perpendicular to the sample surface), as illustrated in Fig. 4(d). This configuration allows the estimation of the width of the EBSD

interaction volume.

Fig. 5 presents a schematic of the relationship between the EBSD interaction volume and the distance from the grain boundary when the EBSD patterns are collected near the edge-on grain boundary. Since the grain boundary is edge-on, the crystal grain distribution in the depth direction can be ignored. When the distance between the grain boundary and the measurement point is greater than the width of the interaction volume, as shown in Figs. 5(a) and (e), a pattern is obtained from a single grain. When the measurement point was located directly on the grain boundary (Fig. 5(c)), the patterns from both grains were mixed. When the distance between the grain boundary and the measurement point is half the width of the interaction volume (Fig. 5(b) and (d)), the mixing of patterns from both sides begins. Therefore, by determining the range in which the patterns from both grains are mixed, the width of the interaction volume can be estimated.

Fig. 6(a) shows an image quality (IQ) map of the virgin sample, acquired with a step size of 5 nm at an accelerating voltage of 15 kV across the edge-on $\Sigma 3$ boundary shown in Fig. 4(b). The grains on the left and right sides correspond to grains A and B, respectively, in Fig. 4(b). The mirror symmetric EBSD patterns, acquired at points B and D in Fig. 6(a), are confirmed in Figs. 6(b) and (d). The pattern shown in Fig. 6(c), acquired at point C, where IQ is lower, reflects a region that includes the grain boundary, exhibiting mixed patterns from both grains. This is evident from the Hough transformation results in the circled areas in Fig. 6(f), which show the presence of bright points corresponding to both patterns in Figs. 6(e) and (g). Edge-on geometry of the boundary was confirmed by the shared band position from $\{111\}$ of both grain A and B, as indicated in Fig. 6(c).

When conducting Spherical Indexing, the similarity between the master pattern of the most likely orientation and the actual pattern is provided by the SCI (Spherical Confidence Index) value in the range

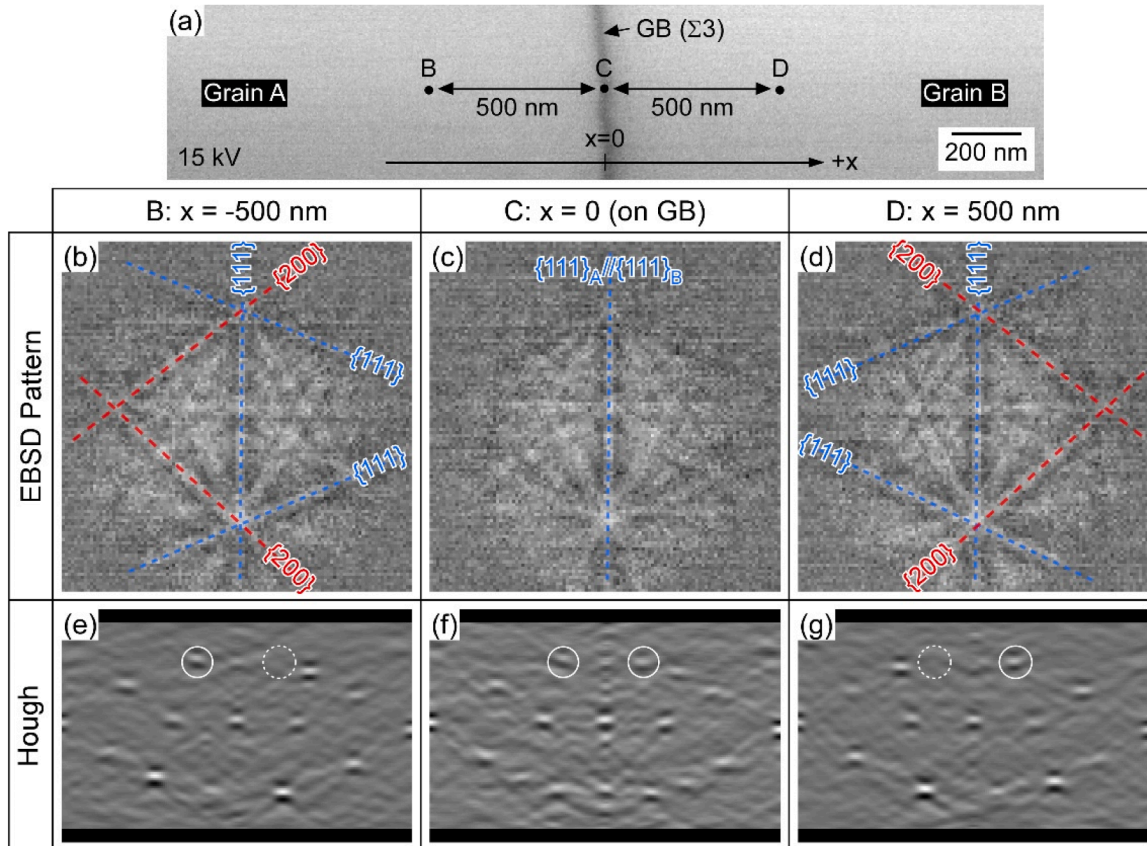


Fig. 6. (a) Image quality (IQ) map of edge-on $\Sigma 3$ boundary of virgin sample taken with accelerating voltage of 15 kV. EBSD patterns obtained from the point (b) B, (c) C, and (d) D, and (e)-(g) results of Hough transformation of the image in (b)-(d).

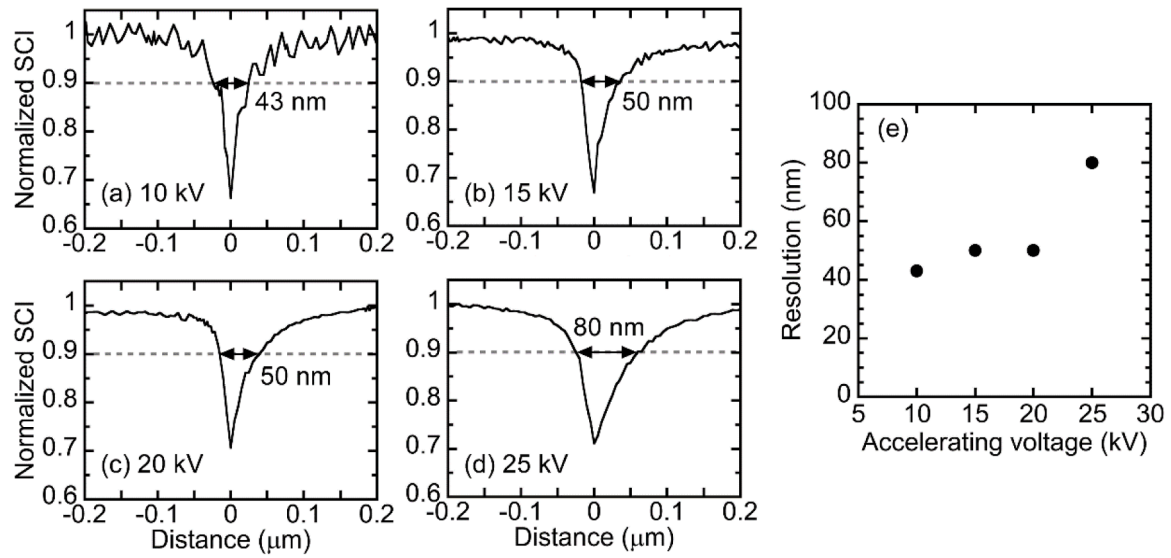


Fig. 7. Relationship between normalized SCI and distance from grain boundary with accelerating voltages of (a) 10 kV, (b) 15 kV, (c) 20 kV, and (d) 25 kV. (e) Relationship between accelerating voltage and special resolution.

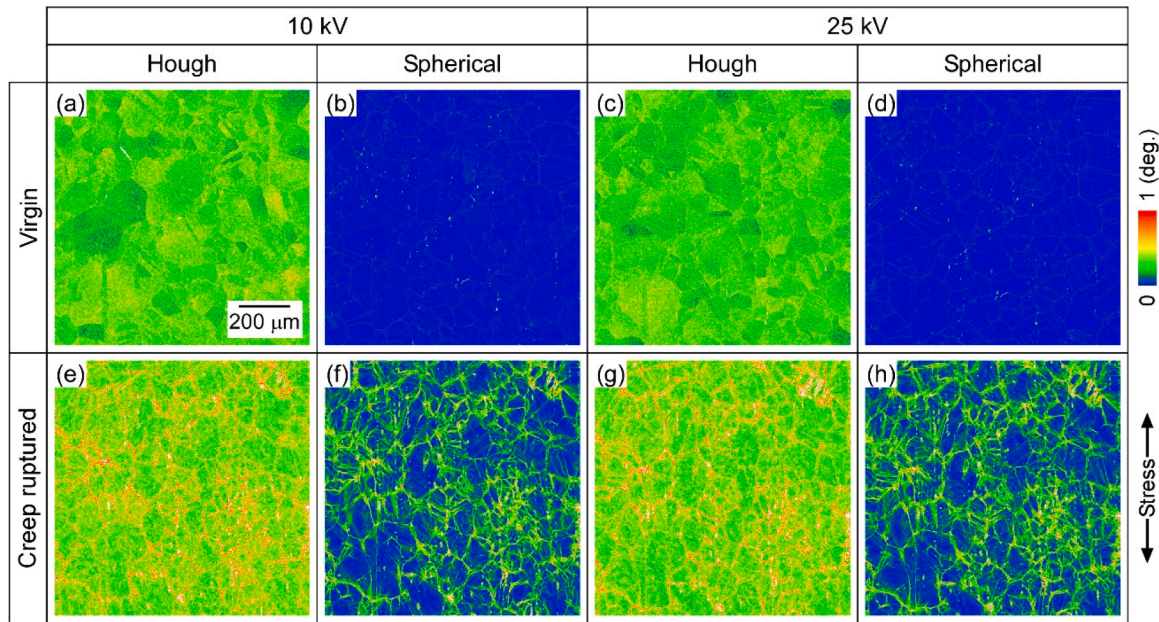


Fig. 8. KAM maps of (a)-(d) virgin and (e)-(h) creep ruptured samples obtained with accelerating voltages of (a)(b)(e)(f) 10, and (c)(d)(g)(h) 25 kV. Indexing was performed by (a)(c)(e)(g) Hough transformation and (b)(d)(f)(h) Spherical Indexing.

from 0 to 1. If patterns from multiple orientations are mixed, the SCI value decreases. In this study, the range across the edge-on $\Sigma 3$ boundary, where mixed patterns occur, was determined based on the SCI value to estimate the spatial resolution.

Figs. 7(a)–(d) show the relationship between the normalized SCI value obtained by Spherical Indexing and the distance from the edge-on $\Sigma 3$ boundary for EBSD patterns acquired with a 5 nm step size at each accelerating voltage. The location where the SCI value is minimized is regarded as the grain boundary ($x = 0$), with negative distances assigned to grain A and positive distances to grain B in Fig. 4(b). The SCI values were normalized so that the average SCI value on the grain A side within a range of $x = 1 \pm 0.05 \mu\text{m}$ from the grain boundary is 1. The profiles were asymmetric, particularly at higher accelerating voltages. It was suggested that a lower SCI on the right side of the grain boundary was caused by the reduced pattern quality owing to the accumulated

contamination by repeated beam exposure with a step size of 5 nm.

Fig. 7(e) shows the relationship between the accelerating voltage and spatial resolution. The threshold value of the pattern mixture from both grains was defined as normalized SCI < 0.9. The threshold was determined based on our previous study [14]. The spatial resolution results are generally consistent with those of previous studies [16], and it was confirmed that lower accelerating voltages lead to improved spatial resolution.

3.3. Effect of accelerating voltage on indexing results

Fig. 8 shows KAM maps of the virgin sample and the creep-ruptured sample indexed by both Hough transformation and Spherical Indexing. To compare the effects of the accelerating voltage, EBSD patterns were acquired from the same field of view at different accelerating voltages.

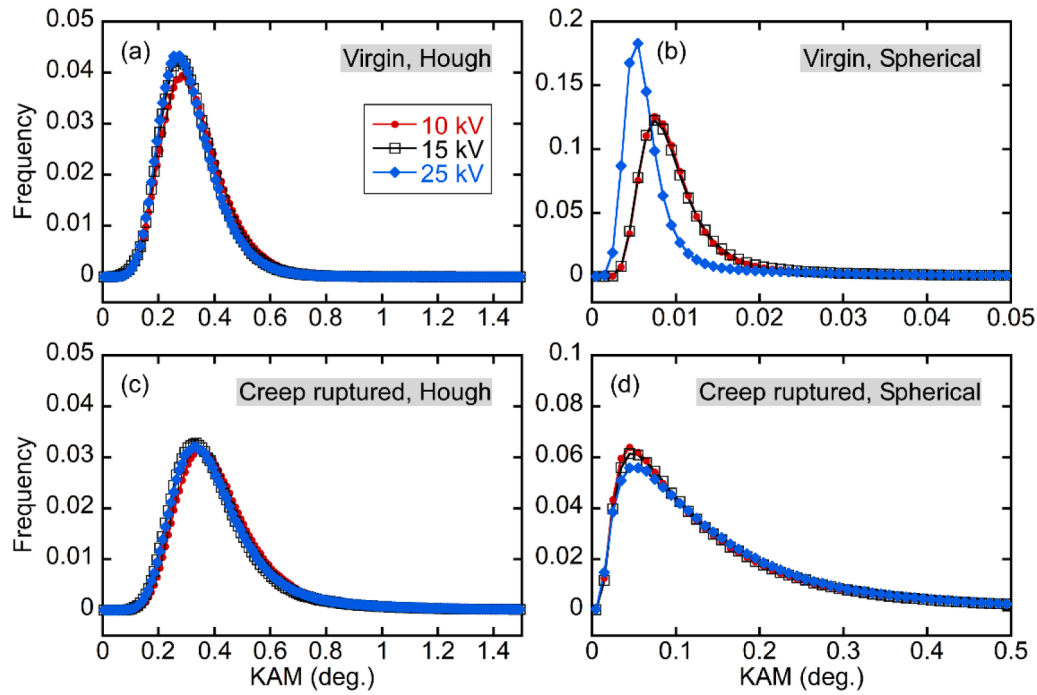


Fig. 9. Histogram of KAM obtained from (a)(b) virgin and (c)(d) creep ruptured samples. Indexing was performed by (a)(c) Hough transformation and (b)(d) Spherical Indexing.

Table 2
Estimated dislocation length in interaction volume.

Dislocation density (m^{-2})	Accelerating voltage (kV)	Interaction volume ($\times 10^{-22} \text{ m}^3$)	Dislocation length in interaction volume (nm)
4×10^{11} (virgin)	10	2.8	0.11
	15	3.8	0.15
	25	9.6	0.38
7×10^{12} (creep ruptured)	10	2.8	1.96
	15	3.8	2.66
	25	9.6	6.72

The measurement area was $1000 \times 1000 \mu\text{m}^2$ with a step size of $1 \mu\text{m}$. The KAM maps were drawn with a maximum value of 1° . When indexed using Spherical Indexing, the KAM values were significantly reduced, indicating that the measurement errors were greatly minimized. Additionally, in the creep-ruptured sample, the KAM values were found to be higher around the grain boundaries. The KAM maps acquired at different accelerating voltages were similar, suggesting that the accelerating voltage does not have a marked effect on KAM.

Fig. 9 shows the effect of the accelerating voltage on the frequency distribution of KAM in both the virgin and creep-ruptured samples, as indexed by the Hough transformation and Spherical Indexing. When using the Hough transformation, the effect of the accelerating voltage was minimal as shown in Fig. 9(a) and (c). In contrast, the virgin sample with Spherical Indexing, there was little change between 10 kV and 15 kV. However, for 25 kV, where the interaction volume was larger (corresponding to lower spatial resolution), the peak of the frequency distribution shifted by approximately 0.002° toward lower angles.

The interaction volume of the EBSD was estimated by assuming a rectangular region defined as (lateral spatial resolution, Fig. 7(e)) \times (vertical spatial resolution = lateral spatial resolution $\times 3$) \times (depth = 50 nm). Geometrically necessary dislocation (GND) density of the virgin and creep-ruptured samples were evaluated to be 4×10^{11} and $7 \times 10^{12} \text{ m}^{-2}$, respectively, from the EBSD results [27] obtained at 15 kV and indexed by Spherical Indexing. Table 2 shows the calculated GND length

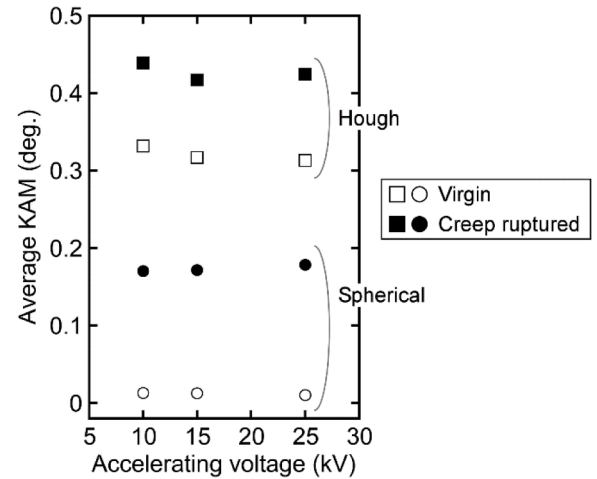


Fig. 10. Average value of KAM as a function of accelerating voltages.

within the interaction volume. In the virgin sample, the GND length within the interaction volume is in the order of the lattice constant of the austenite matrix (0.3599 nm), indicating that almost no dislocations are present. Therefore, under the assumptions made in Fig. 1, the underestimation of misorientation due to the expansion of the interaction volume is negligible in the virgin sample.

The intragranular misorientation in the solution-treated material with a low dislocation density is extremely small, and ideally, KAM should be 0° . Thus, the KAM shown in Fig. 9(a) and (b) likely reflects the measurement error (angular resolution) distribution under each measurement condition. The angular resolutions achieved by Hough indexing and Spherical indexing were identified to be approximately 0.3° and $<0.01^\circ$, respectively. The improved angular resolution at 25 kV can be attributed to the interaction volume being large enough to yield a pattern with sufficient brightness, which increases pattern matching accuracy. In contrast, for the creep-ruptured sample, there are estimated

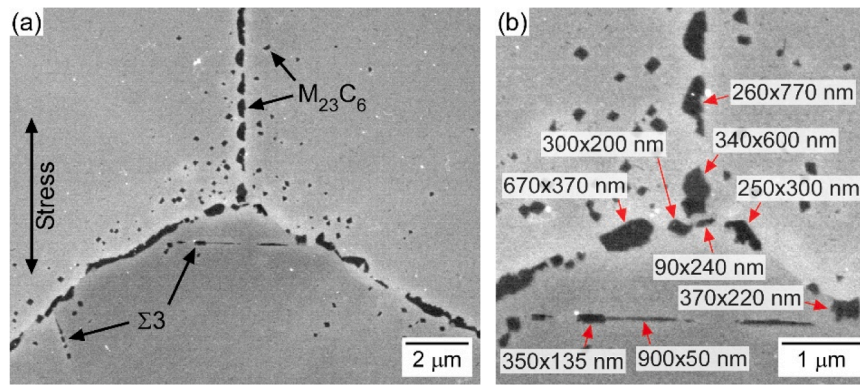


Fig. 11. SEM image of creep ruptured 25Cr-20Ni-Nb-N steel: (a) Lower magnification and (b) Higher magnification around the triple junction.

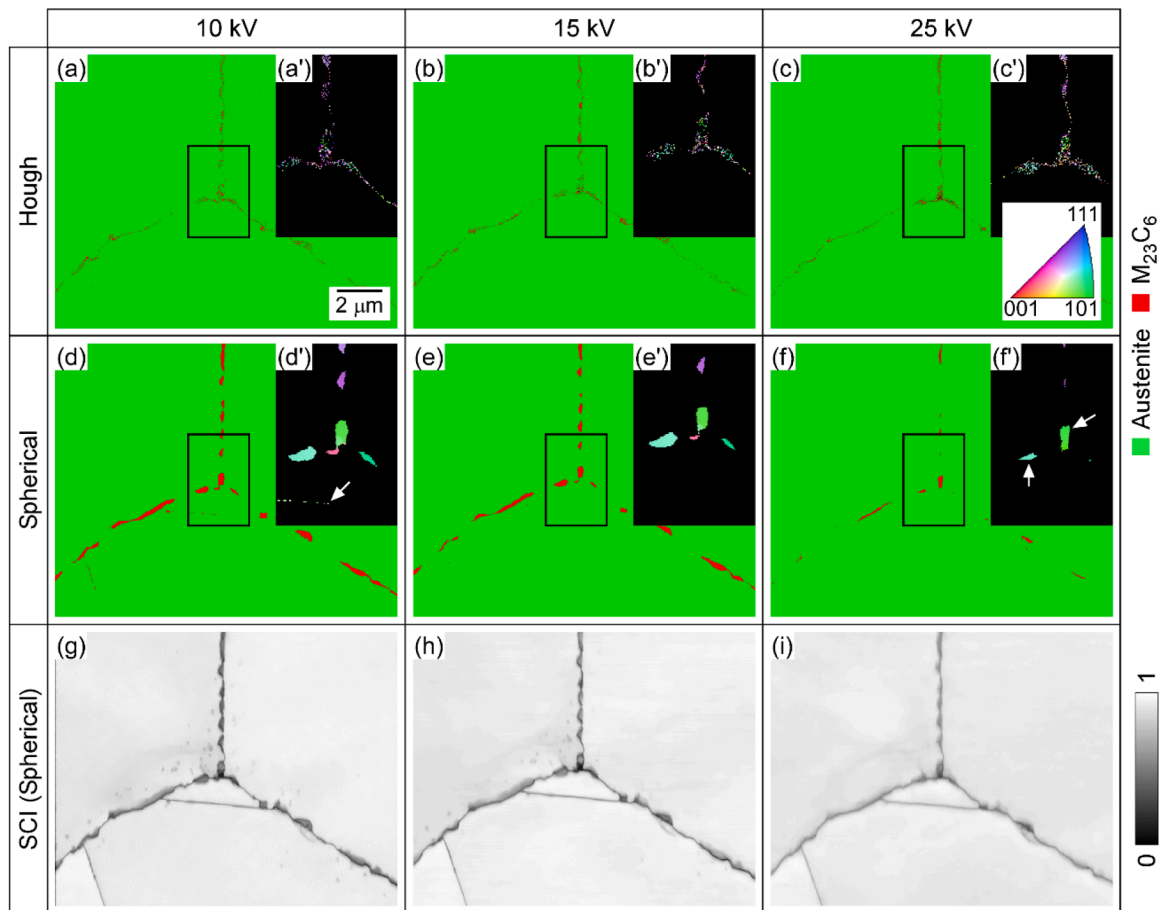


Fig. 12. (a)-(f) Phase maps and (g)-(i) SCI maps of creep ruptured samples obtained with accelerating voltages of (a)(d)(g) 10, and (b)(e)(h) 15 kV, and (c)(f)(i) 25 kV. Indexing was performed by (a)-(c) Hough transformation and (d)-(i) Spherical Indexing. (a')-(f') are IPF maps of $M_{23}C_6$ taken from the rectangle in (a)-(f).

GND lengths of approximately 2–7 nm in the interaction volume. However, as shown in Fig. 9(d), the effect of the accelerating voltage was still minor. This can be explained by the actual misorientations between measurement points being larger, thereby reducing the influence of measurement errors owing to the spatial resolution and pattern qualities.

Fig. 10 shows the effect of the accelerating voltage on the average of all the KAM values obtained in the maps for both samples. The influence of the accelerating voltage on the average KAM was confirmed to be small. When using the Hough transformation, the average KAM increased by approximately 1.5 times from the virgin sample to the creep-ruptured sample. However, with Spherical Indexing, the average

KAM increased by >10 times in the creep-ruptured sample. For creep damage evaluation, the rate of change from the initial material value is a crucial indicator. These results demonstrate the effectiveness of Spherical Indexing-based average KAM as an explanatory variable for creep damage evaluation.

Fig. 11(a) displays an inlens SE image of the creep-ruptured sample, showing that $M_{23}C_6$ precipitates, indicated by black contrast, were found at and near the grain boundaries. Fine $M_{23}C_6$ precipitates were also observed on the $\Sigma 3$ boundaries. Fig. 11(b) shows an enlarged image near the triple junction, with numbers indicating the maximum width (x and y directions) of the precipitates. Their sizes are on the order of several hundred nanometers. EBSD patterns were acquired in the field of

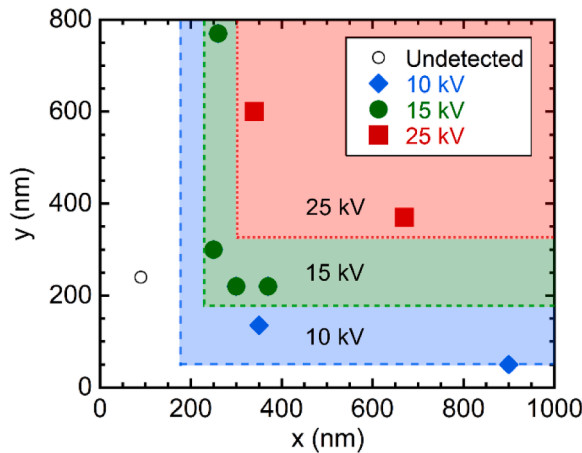


Fig. 13. Detectable size of $M_{23}C_6$ phase by each accelerating voltage.

Fig. 11(a), and the effect of the accelerating voltage on the phase separation of fine precipitates was investigated.

Fig. 12 shows the phase map near the triple junction of the creep-ruptured sample, indexed by both the Hough transformation and Spherical Indexing. Light green indicates austenite and red indicates $M_{23}C_6$. The step size was 25 nm. When using the Hough transformation for indexing, the orientation varied within a single $M_{23}C_6$ particle, and some points were indexed as austenite, indicating poor indexing accuracy, regardless of the accelerating voltage. In contrast, when Spherical Indexing was applied, each $M_{23}C_6$ particle showed consistent orientation, and moderately accurate indexing was achieved.

Comparing the effect of the accelerating voltage when using Spherical Indexing, as indicated by the arrow in Fig. 12(d'), at 10 kV, $M_{23}C_6$ of about 50 nm height on the $\Sigma 3$ boundary was indexed. However, at 25 kV, only two larger $M_{23}C_6$ precipitates (arrow in Fig. 12(f')) were successfully indexed. Although there are other pixels indexed as $M_{23}C_6$, they were considered unsuccessful because the areas indexed as $M_{23}C_6$ were much smaller than the actual size of the precipitates confirmed by SEM. This result indicates that lower accelerating voltages are advantageous for indexing the fine precipitates. However, even at 10 kV, only

$M_{23}C_6$ on the grain boundary was indexed, with intragranular precipitates not being indexed. Although further investigation is required, it is suggested that the ability to index fine precipitates depends not only on the cross-sectional area observed at the sample surface but also on the relationship between the volume of the precipitate, including its depth, and the interaction volume.

At all accelerating voltages, the average SCI value for $M_{23}C_6$ indexed using Spherical Indexing was approximately 0.5–0.6, confirming sufficiently accurate indexing [28]. In the SCI map for 25 kV in Fig. 12(i), the interface between $M_{23}C_6$ on the grain boundary and the matrix was less distinct compared to 10 kV (Fig. 12(g)) and 15 kV (Fig. 12(h)), suggesting that the range where multiple patterns are mixed near the interface was broader. Higher accelerating voltages also resulted in fewer regions of low SCI points near grain boundaries owing to the existence of intragranular $M_{23}C_6$; notably, no low SCI points near grain boundaries were observed at 25 kV. These findings demonstrate that, at 25 kV, the interaction volume was sufficiently large compared to the size of the precipitates, making it impossible to index fine precipitates.

Fig. 13 shows the indexing feasibility for precipitates sized based on the x- and y-directions measured in Fig. 11(b) at each accelerating voltage. For precipitates on the grain boundaries, successful indexing required sizes of approximately 200 nm or greater for 15 kV and 300 nm or greater for 25 kV. At 10 kV, it may be possible to index precipitates smaller than 200 nm, but a sufficient size in the depth direction is considered necessary.

Fig. 14 presents KAM maps of the austenite matrix near the triple junction of the creep-ruptured sample, indexed by Hough transformation and Spherical Indexing. The field of view matches Fig. 12, and the step size was 25 nm. The black particles on the grain boundaries correspond to $M_{23}C_6$. The maximum KAM was set to 1° for Hough transformation and 0.2° for Spherical Indexing. Even when the step size was smaller than the interaction volume, the effect of accelerating voltage on the KAM was minor. Spherical Indexing enabled clearer observation of subtle intragranular orientation variations compared to Hough transformation results, due to reduced impact from measurement error. The elevated KAM values near the grain boundaries highlight that creep deformation occurs preferentially in these areas. Additionally, a region of high KAM running linearly within the upper-right grain was observed; this area was parallel to the (111) slip plane of the austenite

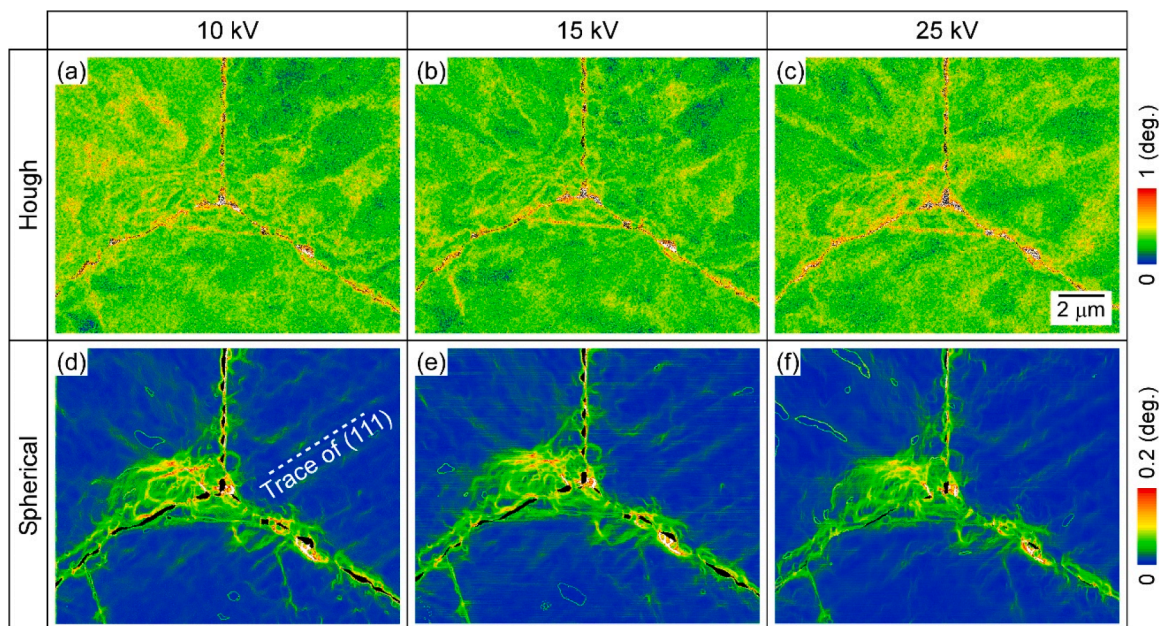


Fig. 14. (a)–(f) KAM maps of creep ruptured samples obtained with accelerating voltages of (a)(d) 10, and (b)(e) 15 kV, and (c)(f) 25 kV. Indexing was performed by (a)–(c) Hough transformation and (d)–(f) Spherical Indexing.

matrix [25], as indicated by the dashed line in Fig. 14(d). While this result is not discussed in detail here, high-precision evaluation of local misorientation using Spherical Indexing suggests the potential for dislocation structure analysis.

4. Conclusions

The effects of the EBSD accelerating voltage on the local misorientation (KAM) and indexing of fine precipitates were investigated using both conventional Hough transformation and novel Spherical Indexing methods. The angular resolutions achieved by Hough indexing and Spherical indexing were identified to be approximately 0.3° and $<0.01^\circ$, respectively. By employing edge-on $\Sigma 3$ boundaries in 25Cr-20Ni-Nb-N steel, it was confirmed that the interaction volume decreased as the accelerating voltage decreased. For the virgin sample with low dislocation density, KAM values indexed by Spherical Indexing at 25 kV were slightly lower; however, when indexed by the Hough transformation, as well as in the creep-ruptured sample with higher dislocation density, no noticeable effect from accelerating voltage was observed. Lower accelerating voltages enabled indexing of finer precipitates in creep-ruptured 25Cr-20Ni-Nb-N steel. At 10 kV, $M_{23}C_6$ precipitates of approximately 50 nm on the $\Sigma 3$ boundaries could be indexed. For indexing precipitates at 15 kV and 25 kV, sizes of approximately 200 nm and 300 nm, respectively, were required.

CRedit authorship contribution statement

Tomotaka Hatakeyama: Writing – original draft, Visualization, Supervision, Resources, Methodology, Investigation, Data curation, Conceptualization. **Kota Sawada:** Writing – review & editing, Resources.

Declaration of competing interest

The authors declare that they have no known competing financial interests or personal relationships that could have appeared to influence the work reported in this paper.

Acknowledgement

Creep test was conducted by Mr. Yasushi Taniuchi, Dr. Kaoru Sekido, and Mr. Takehiro Nojima of the Creep Data Unit, Research Network and Facility Services Division, National Institute for Materials Science. The microstructural observations were conducted with the support of Mr. Taku Moronaga, and Ms. Akiko Nakamura of the Electron Microscopy Unit, Research Network and Facility Services Division, National Institute for Materials Science. This work was partly supported by JSPS KAKENHI Grant number JP25K01536.

Data availability

Data will be made available on request.

References

- [1] S. Suzuki, Features of recent EBSD and its future, *J. Japan Inst. Light Metals* 72 (2022) 570–577, <https://doi.org/10.2464/jilm.72.570>.
- [2] R. Yoda, M. Kamaya, H. Kimura, T. Ohtani, K. Fujiyama, Round Robin test using EBSD for creep damage evaluation, *J. Soc. Mater. Sci., Japan* 66 (2017) 130–137, <https://doi.org/10.2472/jsms.66.130>.
- [3] S.S. Rui, Y.B. Shang, Y.N. Fan, Q.N. Han, L.S. Niu, H.J. Shi, K. Hashimoto, N. Komai, EBSD analysis of creep deformation induced grain lattice distortion: a new method for creep damage evaluation of austenitic stainless steels, *Mater. Sci. Eng. A* 733 (2018) 329–337, <https://doi.org/10.1016/j.msea.2018.07.058>.
- [4] K. Kubushiro, Y. Sakakibara, T. Ohtani, Creep strain analysis of austenitic stainless steel by SEM/EBSD, *J. Soc. Mater. Sci., Japan* 64 (2015) 106–112, <https://doi.org/10.2472/jsms.64.106>.
- [5] K. Kubushiro, Y. Shioda, K. Nomura, Creep degradation for austenitic stainless steel in KA-SUS304J1HTB, *J. Soc. Mater. Sci., Japan* 66 (2017) 179–184, <https://doi.org/10.2472/jsms.66.179>.
- [6] R. Yoda, T. Yokomaku, N. Tsuji, Plastic deformation and creep damage evaluations of type 316 austenitic stainless steels by EBSD, *Mater. Charact.* 61 (2010) 913–922, <https://doi.org/10.1016/j.matchar.2010.05.006>.
- [7] K. Fujiyama, Y. Mizutani, Y. Taniguchi, H. Kimachi, EBSD analysis of creep damage process in SUS304HTB steel, *Zairyo/J. Soc. Mater. Sci., Japan* 62 (2013) 305–310, <https://doi.org/10.2472/jsms.62.305>.
- [8] N.C.K. Lassen, D. Juul Jensen, K. Conradsen, Image processing procedures for analysis of electron back scattering patterns, *Scan. Microsc.* 6 (1992) 115–121.
- [9] Q. Shi, D. Loinsard, Y. Li, Z. Chen, H. Wang, S. Roux, Accuracy assessment of crystal orientation indexations by EBSD, *Meas. Sci. Technol.* 35 (2024) 045030, <https://doi.org/10.1088/1361-6501/ad204d>.
- [10] A.J. Wilkinson, G. Meaden, D.J. Dingley, High-resolution elastic strain measurement from electron backscatter diffraction patterns: new levels of sensitivity, *Ultramicroscopy* 106 (2006) 307–313, <https://doi.org/10.1016/j.ultramicro.2005.10.001>.
- [11] D.J. Rowenhorst, P.G. Callahan, H.W. Ånes, Fast radon transforms for high-precision EBSD orientation determination using *PyEBSDIndex*, *J. Appl. Crystallogr.* 57 (2024) 3–19, <https://doi.org/10.1107/S1600576723010221>.
- [12] W.C. Lenthe, S. Singh, M. De Graef, A spherical harmonic transform approach to the indexing of electron back-scattered diffraction patterns, *Ultramicroscopy* 207 (2019) 112841, <https://doi.org/10.1016/j.ultramicro.2019.112841>.
- [13] R. Hielscher, F. Bartel, T.B. Britton, Gazing at crystal balls: electron backscatter diffraction pattern analysis and cross correlation on the sphere, *Ultramicroscopy* 207 (2019) 112836, <https://doi.org/10.1016/j.ultramicro.2019.112836>.
- [14] T. Hatakeyama, K. Sawada, Effect of lattice parameters of master pattern on EBSD indexing via pattern matching, *J. Japan Inst. Metals Mater.* 90 (2026) 17–26, <https://doi.org/10.2320/jinstmet.J202528>.
- [15] T. Hatakeyama, K. Sawada, Creep damage evaluation of 18Cr–9Ni–3Cu–Nb–N steel by electron backscattered diffraction (EBSD) – comparison of traditional hough indexing and novel spherical indexing –, *Micron* 199 (2025) 103908, <https://doi.org/10.1016/j.micron.2025.103908>.
- [16] D. Chen, J.-C. Kuo, W.-T. Wu, Effect of microscopic parameters on EBSD spatial resolution, *Ultramicroscopy* 111 (2011) 1488–1494, <https://doi.org/10.1016/j.ultramicro.2011.06.007>.
- [17] T. Hatakeyama, K. Sawada, K. Sekido, K. Kimura, Beneficial role of the grain boundary precipitates for intergranular creep fracture of 25Cr–20Ni–Nb–N steel, *Mater. Sci. Eng.: A* 882 (2023) 145487, <https://doi.org/10.1016/j.msea.2023.145487>.
- [18] T. Hatakeyama, K. Sawada, M. Suzuki, M. Watanabe, Microstructure development of modified 9Cr–1Mo steel during laser powder bed fusion and heat treatment, *Addit. Manuf.* 61 (2023) 103350, <https://doi.org/10.1016/j.addma.2022.103350>.
- [19] T. Hatakeyama, A. Kauffmann, S. Obert, C. Gombola, M. Heilmair, K. Yoshimi, Oxidation resistance, creep strength and room-temperature fracture toughness of Mo–28Ti–14Si–6C–6B alloy, *Materialia* 16 (2021) 101108, <https://doi.org/10.1016/j.mtla.2021.101108>.
- [20] V. Tong, J. Jiang, A.J. Wilkinson, T. Ben Britton, The effect of pattern overlap on the accuracy of high resolution electron backscatter diffraction measurements, *Ultramicroscopy* 155 (2015) 62–73, <https://doi.org/10.1016/j.ultramicro.2015.04.019>.
- [21] NIMS creep data sheet No. 58, 2011.
- [22] A. Winkelmann, C. Trager-Cowan, F. Sweeney, A.P. Day, P. Parbrook, Many-beam dynamical simulation of electron backscatter diffraction patterns, *Ultramicroscopy* 107 (2007) 414–421, <https://doi.org/10.1016/j.ultramicro.2006.10.006>.
- [23] P.G. Callahan, M. De Graef, Dynamical electron backscatter diffraction patterns. Part I: pattern simulations, *Microsc. Microanal.* 19 (2013) 1255–1265, <https://doi.org/10.1017/S1431927613001840>.
- [24] T. Hatakeyama, K. Sawada, Precipitation behavior of the M23C6 phase on the coherent twin boundary of 25Cr–20Ni–Nb–N steel, *Mater. Lett.* 363 (2024) 136277, <https://doi.org/10.1016/j.matlet.2024.136277>.
- [25] T. Hatakeyama, K. Sawada, K. Sekido, T. Hara, K. Kimura, Influence of dynamic microstructural changes on the complex creep deformation behavior of 25Cr–20Ni–Nb–N steel at 873 K, *Mater. Sci. Eng. A* 814 (2021) 141270, <https://doi.org/10.1016/j.msea.2021.141270>.
- [26] Y.-Q. Zhang, G.-Z. Quan, J. Zhao, Y.-Z. Yu, W. Xiong, A review on controlling grain boundary character distribution during twinning-related grain boundary engineering of face-centered cubic materials, *Materials* 16 (2023) 4562, <https://doi.org/10.3390/ma16134562>.
- [27] D.P. Field, P.B. Trivedi, S.I. Wright, M. Kumar, Analysis of local orientation gradients in deformed single crystals, *Ultramicroscopy* 103 (2005) 33–39, <https://doi.org/10.1016/j.ultramicro.2004.11.016>.
- [28] W.C. Lenthe, L. Germain, M.R. Chini, N. Gey, M. De Graef, Spherical indexing of overlap EBSD patterns for orientation-related phases – application to titanium, *Acta Mater.* 188 (2020) 579–590, <https://doi.org/10.1016/j.actamat.2020.02.025>.